Frontiers of Information Technology & Electronic Engineering
www.jzus.zju.edu.cn; engineering.cae.cn; www.springerlink.com
ISSN 2095-9184 (print); ISSN 2095-9230 (online)
E-mail: jzus@zju.edu.cn

A *V*-band high-linearity BiCMOS mixer with robust temperature tolerance*

Jiang LUO†1,2, Yizhao LI[1], Yao PENG†‡3, Qiang CHENG†‡2

[1]*School of Electronics and Information Engineering, Hangzhou Dianzi University, Hangzhou 310018, China*

[2]*State Key Laboratory of Millimeter Waves, Southeast University, Nanjing 210096, China*

[3]*Beijing Institute of Radio Measurement, Beijing 100854, China*

†E-mail: luojiang@hdu.edu.cn; pengyao145@126.com; qiangcheng@seu.edu.cn

Received May 10, 2024; Revision accepted July 30, 2024; Crosschecked

Abstract: A high-linearity down mixer with outstanding robust temperature tolerance for *V*-band applications is proposed in this paper. The mixer's temperature robustness has been greatly enhanced by employing a negative temperature-compensation circuit (NTC) and positive temperature-compensation circuit (PTC) in the transconductance (g_m) stage and intermediate frequency (IF) output buffer, respectively. Benefiting from the active balun with enhanced g_m and emitter negative feedback technique, the linearity of the mixer has been significantly improved. For verification, a double-balanced *V*-band mixer was designed and implemented in a 130 nm SiGe BiCMOS process. Measured over the local oscillator (LO) bandwidth from 57 GHz to 63 GHz, the mixer demonstrates a peak conversion gain (CG) of −0.5 dB, a minimal noise figure (NF) of 11.5 dB, and an input 1 dB compression point (IP_{1dB}) of 4.8 dBm under an LO power of −3 dBm. Furthermore, the measurements of CG, NF, and IP_{1dB} exhibit commendable consistency within the temperature range of −55°C to 85°C, with fluctuations of less than 0.8 dB, 1 dB, and 1.2 dBm, respectively. From 57 GHz to 63 GHz, the measured LO-to-radio frequency (RF) isolation is better than 46 dB, the measured return loss at the RF port is >29 dB, and at the LO port it exceeds 12 dB. With a 2.5 V supply voltage, the mixer power consumption is 15.75 mW, 18.5 mW, and 21 mW at temperatures of −55°C, 25°C, and 85°C, respectively. Moreover, the mixer chip occupies a total silicon area of 0.56 mm^2 including all testing pads.

unedited

Key words: *V*-band; Down-conversion mixer; SiGe BiCMOS; Temperature compensation; High-linearity; Active balun
https://doi.org/10.1631/FITEE.2400378 **CLC number:**

1 Introduction

Recently, there has been a growing demand for various wireless applications with high data rates and large bandwidth in the *V*-band (40–75 GHz), such as short-range ultra-high-speed communication (Vardarli et al., 2022; Sutbas et al., 2022), wireless backhaul communication (Mazor et al., 2017), and radar detection (Inanlou et al., 2014; Longhi et al., 2020; Cui et al., 2023), which have attracted widespread attention from academia and industry. Specifically, the 60 GHz band falls within the unlicensed spectrum for commercial wireless communication and is utilized in the WiGig standard (IEEE 802.11ad) (Mazor et al., 2017). It supports multi-gigabit-per-second wireless communication applications, including wireless personal area networks (WPANs) and wireless local area networks (WLANs). In these scenarios, high-performance wireless hardware is essential for achieving the optimal utilization of spectrum resources. As a critical foundational component in receivers, down-conversion mixers

‡ Corresponding authors

* Project supported by the National Key Research and Development Program of China (2023YFB3811503), in part by the Zhejiang Provincial Natural Science Foundation of China (LQ23F040009), in part by the State Key Laboratory of Millimeter Waves, Southeast University (K202316)

ORCID: Jiang LUO, https://orcid.org/0000-0003-4519-792X

© Zhejiang University Press 2024

transform radio frequency (RF) signals into intermediate frequency (IF) or baseband (BB) signals. With the continuous reduction in device size, the silicon germanium (SiGe) BiCMOS process has emerged as a formidable contender against gallium arsenide (GaAs), indium phosphide (InP), and other III–V group compound semiconductor technologies, because it enables cost-effective, highly integrated, and mass-produced millimeter wave (mm-wave) integrated circuits (ICs) (Chen et al., 2020). However, the behavior of silicon-based mixers, including metrics like conversion gain (CG), noise figure (NF), and linearity, can exhibit significant fluctuations with varying ambient temperatures, thereby directly causing deterioration of receiver sensitivity and dynamic range. Therefore, it is highly anticipated that the mixer exhibits excellent robustness against temperature variation.

Many articles focus on mixers that achieve high CG, suppress noise, improve image rejection, and so on (Chou et al., 2012; Kim et al., 2012; Wei et al., 2012; Chiou et al., 2013; Wu et al., 2015; Chi and Chuang, 2016; Kolios and Kalivas, 2016; Choi et al., 2017; Ciocoveanu et al., 2018, 2019a, 2019b; Liu et al., 2018; Kashani et al., 2019; Ahmed et al., 2020; Yu and Kang, 2020; Krishnamurthy et al., 2021; Duan et al., 2023; Yu et al., 2024). In the literature, some publications have reported mixers with temperature-insensitive characteristics. In Yu et al. (2024), a novel passive double-balanced ring structure was employed in a 60–90 GHz mixer-first receiver, achieving high linearity and low local oscillator (LO) leakage. Additionally, two temperature compensation circuits are implemented for the mixer core and IF amplifier, significantly improving the temperature robustness of the receiver. The fabricated prototype supports a wide temperature range, with CG, 1 dB input compression point (IP_{1dB}), and NF variations of less than 1.6 dB, 1.0 dBm, and 2.9 dB, from −20°C to 100°C, respectively. Mazor et al. (2017) reported a highly linear 60 GHz BiCMOS down-conversion mixer with an attenuation mode. For non-attenuation mode, it exhibits a tested CG of 6 dB, a tested input third-order intercept point (IIP3) of 10 dBm, and a tested NF of 12 dB. Despite incorporating temperature bias circuits, the CG, NF, and IIP3 of the mixer still varied by 2.7 dB, 1.9 dB, and 6.1 dBm, respectively, over the temperature range of −40°C to 85°C. To improve process-voltage-temperature (PVT) variations, Ciocoveanu et al. (2018) exploited a self-biasing V_{th} tracking circuit to apply a 60 GHz modified Gilbert-cell mixer fabricated in a 28 nm CMOS technology. The prototype exhibits a CG of 4.7 dB, IP_{1dB} of −3 dBm, and NF of 12.3 dB. The observed changes in the mixer's CG, IP_{1dB}, and NF by 3.6 dB, 2.4 dBm, and 2.7 dB, respectively, across the temperature range of −30°C to 120°C, indicates considerable room for improvement. More recently, a 76–81 GHz transceiver with bidirectional mixer was designed for automotive radar applications (Duan et al., 2023). By employing multiple temperature compensation techniques, this millimeter-wave transceiver chip demonstrates good temperature robustness ranging from −45°C to 125°C, achieving an NF of 11.2 dB, IP_{1dB} of −7 dBm, and an output power of 14.5 dBm. Several *V*-band mixers developed in CMOS technology have been reported (Chou et al., 2012; Wei et al., 2012; Chiou et al., 2013; Choi et al., 2017; Kashani et al., 2019; Krishnamurthy et al., 2021). A down-conversion mixer operating at 60 GHz was developed employing active balun and transconductance linearization methods (Choi et al., 2017). The mixer delivers a CG of 5.6 dB, IP_{1dB} of −7 dBm, an output third-order intercept point (OIP3) of 12.4 dBm, and an NF of 10.9 dB. Kashani et al. (2019) reported a *V*-band low-noise mixer-first architecture. A revised single-balanced configuration serves as the mixer's core, enhancing both the CG and NF while maintaining power efficiency and linearity. The fabricated mixer achieves a maximum CG of 12.1 dB, minimum NF of 6.5 dB, IP_{1dB} value of −5 dBm, and a low core power consumption of 3 mW. Some other high linearity silicon mixers are reported. They achieve an IP_{1dB} of −7 dBm (Chou et al., 2012), −6 dBm (Wei et al., 2012), −1 dBm (Chiou et al., 2013) and −2 dBm (Krishnamurthy et al., 2021), respectively. Based on the literature mentioned above, the main challenge in designing high-performance millimeter-wave mixers lies in balancing the trade-offs between CG, NF, linearity, and power consumption under wide temperature operating conditions. Therefore, there is a significant demand for new approaches that can achieve robust overall performance while being insensitive to temperature variations.

In this study, a *V*-band down-conversion mixer

Unedited

was designed and implemented using a 130 nm SiGe BiCMOS process. A negative temperature-compensation circuit (NTC) and a positive temperature-compensation circuit (PTC) are respectively applied to the mixer's transconductance (g_m) stage and IF output buffer to achieve excellent wide temperature tolerance. The incorporation of emitter negative feedback and active balun with enhanced g_m greatly improved the mixer's linearity. The proposed design techniques have been validated in a *V*-band mixer, demonstrating excellent temperature robustness and high linearity. This paper is organized as follows: Section 2 focuses on the design and implementation of the *V*-band mixer. The following Section 3 presents the measurement results to validate the design. Finally, conclusions are presented in Section 4.

2 Circuit Analysis and Design

Fig. 1 illustrates the architecture of the proposed *V*-band down-conversion mixer, featuring a double-balanced Gilbert-cell mixer core, an output IF buffer equipped with an active balun, a PTC module, an NTC module, and two Marchand RF/LO baluns. RF/LO baluns perform single-to-differential rotation and ensure 50 Ω matching at the input ports RF/LO, respectively. The mixer core employs a double-balanced Gilbert cell, primarily consisting of the switching stage, transconductance (g_m) stage with inductive degeneration, and *RC* load stage. The switch stage consists of two pairs of NPN-type heterojunction bipolar transistors (HBTs) T_1 and T_2 and T_3 and T_4, driven by a differential LO signal. The two pairs of HBTs operate at low overdrive voltages, thereby reducing the required LO injection power. The g_m stage comprises two HBTs T_5 and T_6 along with two negative feedback inductors L_1 and L_2. This implementation improves linearity and expands the bandwidth. The load stage is composed of two parallel resistor and capacitor pairs, namely R_1 and R_2 and C_1 and C_2, which effectively filter out high-frequency interference and enhance LO suppression at the IF terminal. The active balun composed of n-type metal-oxide-semiconductor field-effect transistors (MOSFETs) M_1 and M_2 serves as a differential-to-single IF output buffer, while also further enhancing the linearity of the mixer. To achieve wide temperature operation characteristics, two temperature compensation circuits are employed. An NTC module is utilized to generate a negative temperature coefficient bias current, applied to the base nodes of g_m stage T_5 and T_6 through bias resistors R_7 and R_8, achieving temperature compensation for its g_m. Additionally, a PTC circuit is used to output a positive temperature coefficient bias voltage, applied to the active balun, thereby effectively compensating the output IF buffer. Fig. 1 displays the optimized dimensions of the key active device and the values of passive elements for the proposed mixer.

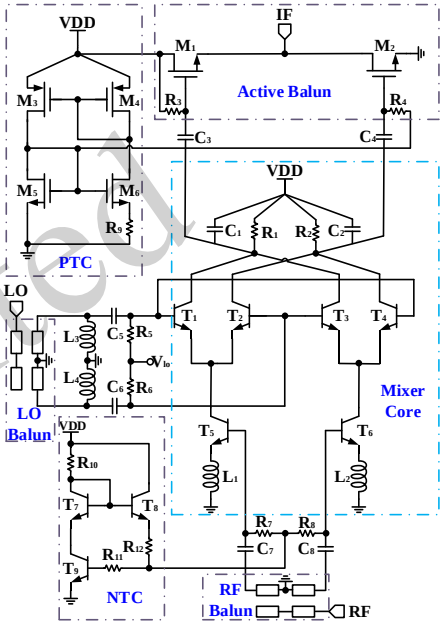

M_1,M_2	256μm/1.2μm	R_1,R_2	146Ω	C_1,C_2	500fF
M_3	4.8μm/1μm	R_3,R_4	569kΩ	C_3,C_4	30pF
M_4	4μm/1μm	R_5,R_6	519Ω	C_5,C_6	260fF
M_5	2μm/1μm	R_7,R_8	187Ω	C_7,C_8	200fF
M_6	16μm/1μm	R_9,R_{10}	13.6kΩ/1.4kΩ	L_1,L_2	115pH
T_1~T_6	120nm/4μm	R_{11},R_{12}	3.2kΩ/670Ω	L_3,L_4	90pH

Fig. 1. Schematic of the proposed *V*-band mixer.

2.1 Negative temperature coefficient compensation circuit

Due to inherent factors of silicon-based processes, characteristics of active devices such as g_m and threshold voltage vary with environmental temperature changes. As depicted by the blue curve in Fig. 2, in the absence of temperature compensation circuits, the mixer's CG sharply increases with temperature elevation and eventually stabilizes.

Unedited

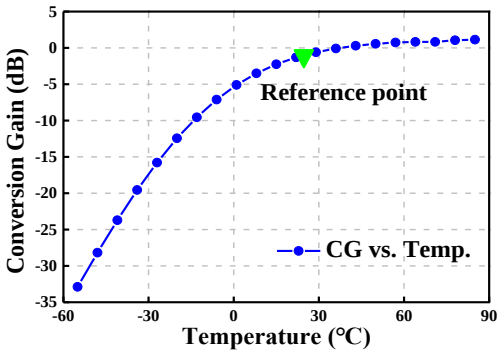

Fig. 2. Simulated results of CG vs. temperature variation. CG, conversion gain.

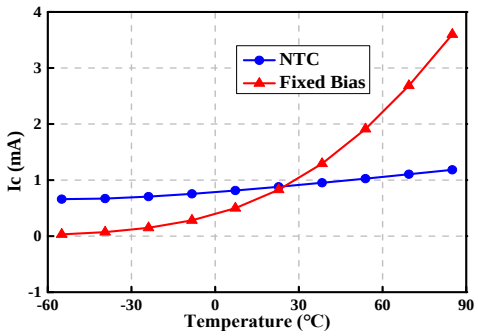

Fig. 3. Simulated collector current of g_m stage transistors vs. temperature variation.

1. Set the reference point

✧Simulate the gain over the desired temperature range (−55~85℃)

✧Select the gain at room temperature (25℃) as the reference point

2. Simulate the best bias voltage curve

✧Adjust bias voltage to minimize gain deviation from the reference value reference at −55 to 85℃

3. Design the best bias generation circuit

✧Design the optimal bias circuit for temperature compensation

Fig. 4. The three-step process for designing a temperature compensation circuit.

Compared with MOSFET devices, HBT devices are more sensitive to temperature variations. Therefore, the first consideration is to introduce a compensation circuit in the g_m stage composed of T_5 and T_6. As shown by the red curve in Fig. 3, the collector current of the g_m stage transistors increases significantly with ambient temperature. CG is directly associated with the collector current. Thus, temperature compensation for CG can be achieved by generating a negative temperature coefficient base current to reduce the fluctuation of the collector current (Razavi, 2001). Based on this idea, Fig. 4 outlines the design process for implementing a temperature compensation circuit through a three-step procedure.

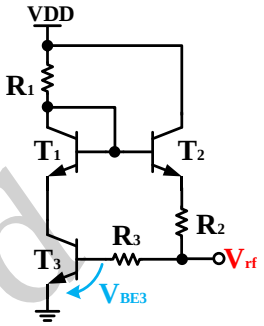

Fig. 5. The proposed negative temperature coefficient compensation circuit.

As illustrated in Fig. 5, the circuit is implemented using transistors T_1–T_3 and resistors R_1–R_2. The derivation of NTC is as follows. The collector current for the HBT device T_3 can be expressed as follows:

$$I_{c3} = I_{s3} \exp(\frac{V_{BE3}}{V_T}), \quad (1)$$

where $V_T = KT/q$, and the saturation current $I_{s3} \propto \mu KT n_i^2$. Here, μ represents carrier mobility and n_i denotes the intrinsic carrier concentration of silicon. The relationship between these parameters and temperature can be expressed as $\mu \propto \mu_0 T^2$, where $m \approx -1.5$ and $n_i^2 \propto T^3 \exp(-E_g/KT)$. In this design, the E_g of HBT is approximately 1 eV, and the saturation current can be represented as:

$$I_{s3} = bT^{4+m} \exp(\frac{-E_g}{KT}), \quad (2)$$

where b is a proportional factor, and the output voltage V_{rf} can be written as:

unedited

$$V_{rf} = V_{BE3} = V_T \ln(\frac{I_{c3}}{I_{s3}}). \quad (3)$$

The output voltage V_{rf} is determined by the voltage between the base and emitter of transistor T_3. To simplify the analysis, we can temporarily assume that I_{c3} remains unchanged, as follows:

$$\frac{\partial V_{BE3}}{\partial T} = \frac{\partial V_T}{\partial T} \ln(\frac{I_{c3}}{I_{s3}}) - \frac{V_T}{I_s} \frac{\partial I_{s3}}{\partial T}. \quad (4)$$

The partial derivative of saturated current in Eq. (2) is:

$$\frac{\partial I_{s3}}{\partial T} = bT^{3+m} \exp(\frac{-E_g}{KT})(4 + m + \frac{E_g}{KT}). \quad (5)$$

Based on Eqs. (4) and (5), the partial derivative of the output voltage with respect to temperature is,

$$\frac{\partial V_{rf}}{\partial T} = \frac{V_{BE3} - (4 + m)V_T - \frac{E_g}{q}}{T}. \quad (6)$$

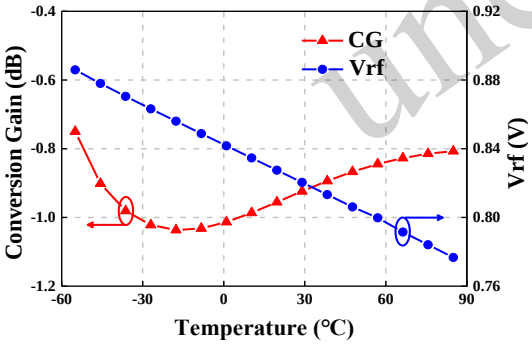

Fig. 6. Simulated results of temperature variation vs. CG and output voltage V_{rf}. CG, conversion gain.

Eq. (6) provides the temperature coefficient of the voltage difference between the base and emitter, namely the output voltage V_{rf}, at a given temperature. From this equation, we can observe its dependency on V_{BE3}. When $V_{BE3} \approx 820$ mV and $T = 300$ K, the temperature coefficient is around −0.8 mV/°C. As plotted by the blue curve in Fig. 6, the output voltage V_{rf} exhibits negative temperature characteristics, consistent with the derivation mentioned above. By utilizing the designed NTC, the output voltage V_{rf} gradually decreases as the temperature rises. The V_{rf} is applied to the g_m stage, effectively suppressing the increase in collector currents of transistors T_5 and T_6. Fig. 3 illustrates the variation trends of the collector currents of transistors T_5 and T_6 with and without an NTC. Consequently, this achieves temperature compensation for the g_m stage.

2.2 Positive temperature coefficient compensation circuit

Due to intrinsic factors within the NMOSFET device, the g_m of NMOSFET devices decreases with increasing temperature, thereby reducing the gain of the output IF buffer (Wang *et al.*, 2023). By increasing the bias voltage of the MOSFET transistors, the g_m can be enhanced to compensate for the gain.

The proposed PTC, as depicted in Fig. 7a, represents a self-biased current source generation circuit. It comprises a linear current source formed by PMOSFET transistors MP_3 and MP_4 and a nonlinear current source constituted by NMOSFET transistors MN_1–MN_2 along with resistor R. The ratio of width to length between MP_3 and MP_4 is K:1, and the ratio of width to length between MN_2 and MN_1 is N:1, with both K and N being >1.

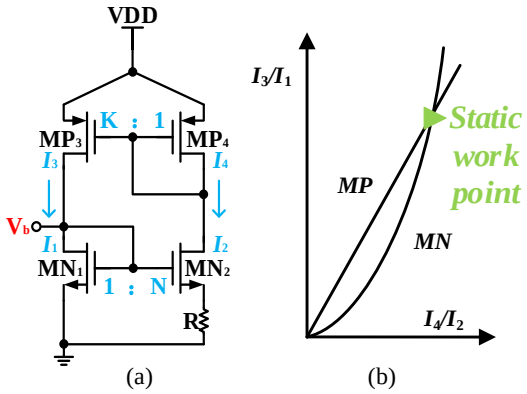

Fig. 7. (a) Positive temperature coefficient compensation circuit and (b) static working point

The static operating point diagram of the self-biased current source circuit is shown in Fig. 7b. The line MP represents the current variation on MP_3 and MP_4 in the linear current source, with a slope equal to the current ratio K:1 of MP_3 to MP_4. The curve MN represents the current variation on MN_2 and MN_1 in the nonlinear current source, with a slope

unedited

equal to the reciprocal of the current ratio of MN_2 to MN_1. This slope variation includes both positive and negative feedback. Initially, the current in the branch is very small, and the voltage drop across the resistor R can be neglected. MN_2 copies the current from MN_1 to the right branch in an N:1 ratio, and then MP_3 copies the current from MP_4 to the left branch in a K:1 ratio, which constitutes positive feedback. As the current increases, the voltage drop across the resistor cannot be ignored. The resistor starts to provide negative feedback, weakening the ability of MP_3 to replicate the current. Eventually, MP and MN will have two intersection points, and the non-zero intersection point is called the static operating point.

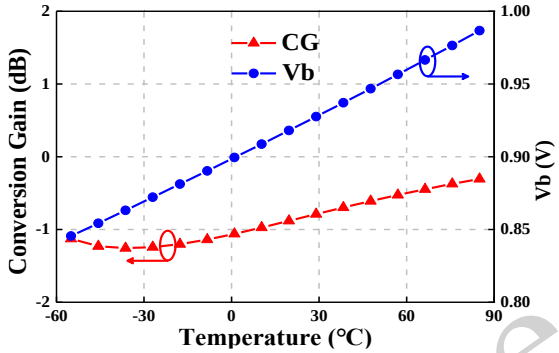

Fig. 8. Simulated results of temperature vs. CG and bias voltage. CG, conversion gain.

The ratio of the current in the left branch to the current in the right branch is K:1. Neglecting the body effect and assuming the current in the right branch is I, the formula for the current-voltage relationship in the saturation region of the left branch is

$$KI = \frac{1}{2}\mu C_{ox}(W/L)_1(V_{GS1} - V_{TH})^2. \quad (7)$$

From Eq. (7), we can obtain

$$V_{GS1} = \sqrt{\frac{2KI}{\mu C_{ox}(W/L)_1}} + V_{TH}. \quad (8)$$

According to Kirchoff's voltage law (KVL) equation, we can write

$$V_{GS1} = V_{GS2} + IR, \quad (9)$$

which gives

$$\sqrt{\frac{2KI}{\mu C_{ox}(W/L)_1}} + V_{TH} = \sqrt{\frac{2I}{\mu C_{ox}(W/L)_2}} + V_{TH} + IR, \quad (10)$$

$$I = \frac{2}{\mu C_{ox}(W/L)_1}\frac{1}{R^2}(\sqrt{K} - \frac{1}{\sqrt{N}})^2. \quad (11)$$

By combining Eq. (7) and taking the partial derivative with respect to temperature T, we can obtain

$$\frac{\partial V_b}{\partial T} = \frac{\partial V_{GS1}}{\partial T} = \frac{2Km(1-\frac{1}{\sqrt{KN}})(\frac{T}{T_0})^{-m-1}}{\mu(T_0)T_0C_{ox}(W/L)_1R} + \frac{\partial V_{TH}}{\partial T}. \quad (12)$$

where m lies in the range 1.5–2, and T_0 is the reference temperature. The left term in the equation is >0. By selecting appropriate values for K, N, and R, the positive temperature compensation bias voltage shown in Fig. 8 can be obtained. As shown in Fig. 8, the PTC generates an output voltage that increases as the temperature rises to compensate for the g_m of the buffer, thereby stabilizing the CG.

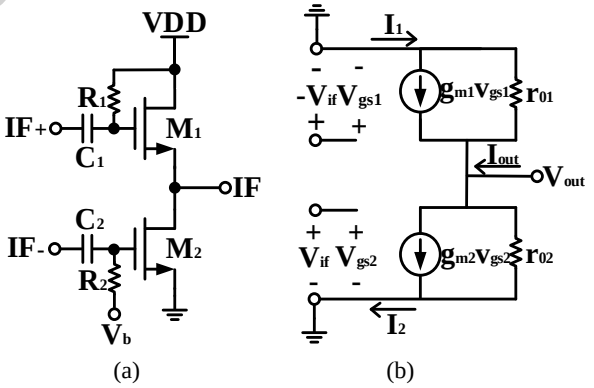

Fig. 9. (a) Schematic of active balun and (b) its small signal equivalent model

2.3 Active Balun

The active balun proposed in Fig. 9a serves as an output IF buffer while converting from differential to single-ended signals, achieving impedance matching and high linearity simultaneously. To ensure good linearity, both transistors M_1 and M_2 are required to operate in saturation. The equivalent small-signal model of the active balun is shown in Fig. 9b. By analyzing the small-signal model, the current can be

Unedited

calculated as follows:

$$I_1 = g_{m1}V_{gs1} + \frac{V_{gs1}}{r_{o1}} = -g_{m1}V_{if} - \frac{V_{if}}{r_{o1}},$$
$$I_2 = g_{m2}V_{gs2} + \frac{V_{gs2}}{r_{o2}} = g_{m2}V_{if} + \frac{V_{if}}{r_{o2}}. \quad (13)$$

The output current can be expressed as

$$I_{out} = I_1 - I_2 = -V_{if}\left(g_{m1} + g_{m2} + \frac{1}{r_{o1}} + \frac{2}{r_{o2}}\right). \quad (14)$$

As demonstrated in Eq. (14), the common source and common drain configuration are employed to enhance the output current I_{out} and the output voltage swing, thus improving the linearity.

3 Experimental Results and Discussion

The proposed *V*-band double-balanced down-conversion mixer with excellent temperature robustness was designed and fabricated in a 130 nm SiGe BiCMOS, which is a high-performance technology that is compatible with the 130 nm CMOS process. The NPN-type HBT transistor for RF applications achieves a cutoff frequency f_T around 260 GHz and a maximum oscillation frequency f_{MAX} around 320 GHz, respectively. To achieve the more accurate performance of the mixer, passive components including baluns, inductors, capacitors, testing pads, interconnections, vias, and more, were optimized through a full-wave three-dimensional electromagnetic field simulator and circuit co-simulations. A die microphotograph of the *V*-band mixer chip is shown in Fig. 10. The whole chip area including two on-chip transformer baluns and all testing pads is 0.56 mm^2.

Utilizing a probe station (MPI TS200-SE) equipped with ground-signal-ground (G-S-G) probes with a pitch of 150 μm, on-wafer *S*-parameter measurements were conducted within the 57–63 GHz frequency range. This setup was complemented by a Keysight PNA-X-N5247B network analyzer, supporting NF applications, and a Keysight N6705C DC power analyzer renowned for its high resolution. Calibration was achieved through the standard short-open-load-through (SOLT) method. The proposed mixer's temperature characterization employs the AC3 Fusion thermal chuck system from ERS electronic GmbH to regulate the ambient temperature of the probe station. It accommodates operating temperatures ranging from −65°C to 400°C, offering a temperature accuracy of ±0.1°C and a display resolution of 0.01°C.

Fig. 11 illustrates the simulated and measured variations of CG vs. LO frequency for the mixer at temperatures of −55°C, 25°C, and 85°C, respectively. With the IF frequency fixed at 0.1 GHz, the RF frequency ranges from 56.9 GHz to 62.9 GHz, while the LO frequency under −3 dBm injection power varies from 57 GHz to 63 GHz. It can be seen that the CG variation remains less than ±0.4 dB from 57 GHz to 63 GHz, corresponding to ±0.0028 dB/°C. The consistency among these measured data indicates the effectiveness of the proposed temperature compensation technique. The simulated and measured results exhibit good agreement.

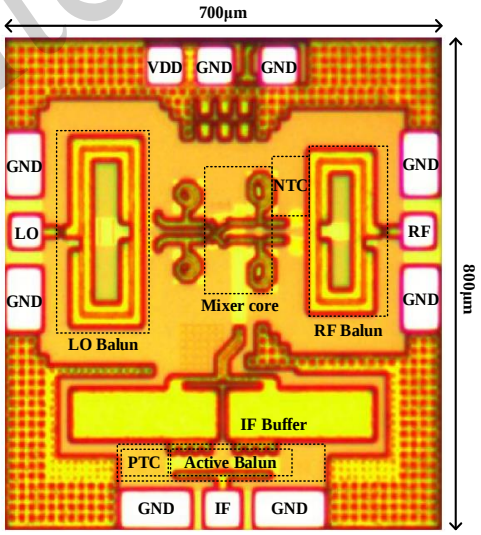

Fig. 10. Die micrograph of the proposed *V*-band mixer.

The Keysight PNA-X-N5247B network analyzer, equipped with NF functionality, was also employed to evaluate the NF metrics of the mixer chip. In Fig. 12, the simulated and measured NF results are depicted. Within the target frequency range of 57–63 GHz, the measured NFs demonstrate good flatness, with variations of <1 dB. For instance, at room temperature (25°C), the measured NF increases from 11.5 dB to 12 dB. Across all test temperatures, the variation in NF is better than ±0.5 dB. The power-handling capa-

unedited

bility with the LO frequency from 57 GHz to 63 GHz of the mixer is presented in Fig. 13. Benefiting from the employed emitter negative feedback and active balun technology with transconductance enhancement, the measured input 1 dB compression point (IP_{1dB}) exceeds 3.9 dBm within the frequency band of interest, while the variation in IP_{1dB} at different operating temperatures is less than ±0.6 dBm. All measurements presented previously were conducted within a temperature range from −55°C to 85°C.

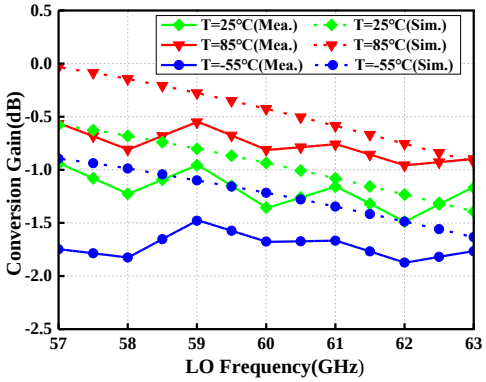

Fig. 11. Measured and simulated CG under −55 °C, 25 °C, and 85 °C, respectively. CG, conversion gain.

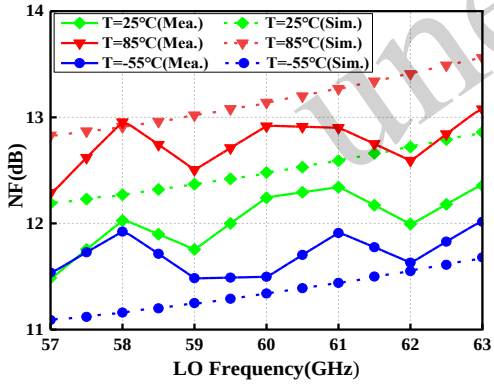

Fig. 12. Measured and simulated NF under −55 °C, 25 °C, and 85 °C, respectively.

The measured isolation from the LO port to the RF port and the return losses at both the LO and RF ports are depicted in Fig. 14. It is evident from Fig. 14 that the isolation between the LO and RF ports exceeds 46 dB within the bandwidth of 57–63 GHz. Within the measured frequency range of interest, the measured return loss at the RF port is better than 29 dB, while at the LO port, it is >12 dB. Operating at a supply voltage of 2.5 V, the mixer exhibits DC power consumption of 15.75 mW, 18.5 mW, and 21 mW at temperatures of −55°C, 25°C, and 85°C, respectively.

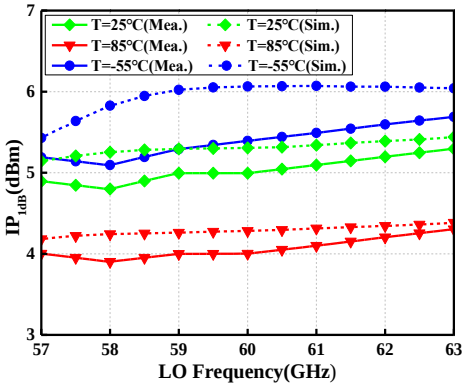

Fig. 13. Measured and simulated IP_{1dB} under −55 °C, 25 °C, and 85 °C, respectively.

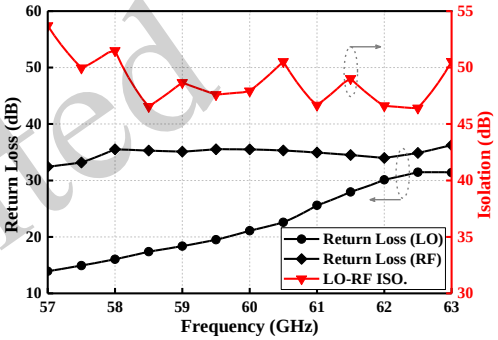

Fig. 14. Measured return loss and isolation for LO frequencies from 57 to 63 GHz. LO, local oscillator.

Table 1 summarizes the performance of the proposed *V*-band mixer and recently reported CMOS/SiGe BiCMOS mixers. The proposed mixer demonstrates outstanding temperature robustness by incorporating PTC and NTC temperature compensation techniques, allowing it to maintain excellent overall performance under wide temperature operation. Within the temperature range of −55°C to 85°C, the measured CG, NF, and IP_{1dB} variations are better than 0.8 dB, 1 dB, and 1.2 dBm, respectively. Compared with the recently reported mixers, the proposed mixer exhibits competitive performance of wide temperature characteristics, high linearity, and low power consumption.

4 Conclusion

A positive and negative temperature compensation technique was developed and successfully imple-

Unedited

Table 1 Performance summary and comparison with recently reported mixers

Ref.	Temp. (°C)	Process	Freq. (GHz)	P_{LO} (dBm)	CG (dB)	NF (dB)	IP_{1dB} (dBm)	LO-RF ISO. (dB)	Power (mW)	Area (mm^2)
Mazor *et al*., 2017	−55~85	130 nm SiGe	57~66	0	6.1~ 8.8*	11.4~ 13.3*	−9.5~ −3.4*	>46*	55^	0.47
Yu *et al*., 2024	−20~100	28 nm CMOS	60~90	N/A	16~ 18.4	7.5~ 11.2	−4~ −5	>35.8	41.5^	0.46
Ciocoveanu *et al*., 2018	−30~120	28 nm CMOS	60	−2	2.9~ 6.5#	11~ 13.7#	−4.2~ −1.8#	N/A	1.8^	0.24
Duan *et al*., 2023	−45~125	65 nm CMOS	76~83	N/A	26~ 68$	11.2~ 12.5	−7	N/A	N/A	0.85
This work	−55~85	130 nm SiGe	57~63	−3	−1.6~ −0.8	11.5~ 12.5	4~ 5.2	>46	15.7~ 21	0.56

#Post-layout simulation results, *Chart estimation, ^Room temperature, $With low NF amplifier

mented in a *V*-band down-conversion mixer using a 130 nm SiGe BiCMOS process. This advancement enables the mixer to maintain consistent CG, NF, and linearity during large ambient thermal variation. In the temperature span from −55°C to 85°C, the variations in CG, NF, and IP_{1dB} measurements are all superior to 0.8 dB, 1 dB, and 1.2 dBm, respectively. The incorporation of emitter negative feedback and an active balun has greatly improved the mixer's linearity. Consequently, within the frequency range of 57–63 GHz, the measured IP_{1dB} exceeds 5.1 dBm, 4.8 dBm, and 3.9 dBm at temperatures of −55°C, 25°C, and 85°C, respectively. Furthermore, at temperatures of −55°C, 25°C, and 85°C, the mixer consumes DC power of 15.75 mW, 18.5 mW, and 21 mW, respectively. The proposed mixer exhibits performance that is competitive with those of other mixers and therefore has potential as a building component for millimeter-wave ultra-high-speed communication transceivers.

Contributors

Conceptualization, Jiang LUO and Yao PENG; Methodology, Jiang LUO and Yizhao LI; Writing - original draft, Yizhao LI; Writing - review & editing, Jiang LUO, Yao PENG, and Qiang CHENG; Supervision, Yao PENG and Qiang CHENG. All authors have read and agreed to the published version of the manuscript.

Conflict of interest

All the authors declare that they have no conflict of interest.

Data availability

The data that support the findings of this study are available from the corresponding author upon reasonable request.

References

Ahmed A, Huang MY, Munzer D, et al., 2021. A 43-97-GHz mixer-first front-end with quadrature input matching and on-chip image rejection. *IEEE J Solid-State Circuits*, 56(3):705-714. https://doi.org/10.1109/JSSC.2020.3045046

Chen JD, Qian JB, Huang SY, 2020. A low-noise and high-gain folded mixer for a UWB system in 0.18-μm SiGe BiCMOS technology. *IEEE Trans Circuits Syst II: Express Briefs*, 68(2):612-616. https://doi.org/10.1109/TCSII.2020.3019486

Chi CH, Chuang HR, 2016. A 60-GHz CMOS ultra-low-power single-ended sub-harmonic mixer in 90-nm CMOS. Proc IEEE International Symposium on Radio-Frequency Integration Technology, p.1-3. https://doi.org/10.1109/RFIT.2016.7578179

Chiou HK, Chou HT, Liang CJ, 2013. A 35-to-83 GHz multiconductor-lines signal combiner for high linear and wideband mixer. *IEEE Microwave Wireless Compon Lett*, 23(10):548-550. https://doi.org/10.1109/LMWC.2013.2279099

Choi C, Son JH, Lee O, et al., 2017. A +12-dBm OIP3 60-GHz RF Downconversion mixer with an output-matching, noise- and distortion-canceling active Balun for 5G applications. *IEEE Microwave Wireless Compon Lett*, 27(3):284286. https://doi.org/10.1109/LMWC.2017.2661964

Chou HT, Liang JR, Chiou HK, 2012. V-band low-power Darlington-pair gate-pumped mixer with thin-film LC-hybrid linear combiner in 90 nm CMOS. *Electron Lett*, 48(16):1023-1024. https://doi.org/10.1049/el.2012.1690

Ciocoveanu R, Rimmelspacher J, Weigel R, et al., 2018. A 1.8-mW low power, PVT-resilient, high linearity, modified Gilbert-cell down-conversion mixer in 28-nm CMOS. Proc IEEE 18th Topical Meeting on Silicon Monolithic

Unedited

Integrated Circuits in RF Systems, p.19-22. https://doi.org/10.1109/SIRF.2018.8304218

Ciocoveanu R, Weigel R, Issakov V, 2019a. A highly integrated 60 GHz receiver for radar applications in 28 nm bulk CMOS. Proc IEEE International Conf on Microwaves, Antennas, Communications and Electronic Systems, p.1-5. https://doi.org/10.1109/COMCAS44984.2019.8958434

Ciocoveanu R, Weigel R, Hagelauer A, et al., 2019b. Modified gilbert-cell mixer with an LO waveform shaper and switched gate-biasing for 1/f noise reduction in 28-nm CMOS. *IEEE Trans Circuits Syst II: Express Briefs*, 66(10):1688-1692. https://doi.org/10.1109/TCSII.2019.2923595

Cui J, LI PP, Sheng WX, 2023. High linearity U-band power amplifier design: a novel intermodulation point analysis method. *Front Inform Technol Electron Eng*, 24(1):176-186. https://doi.org/10.1631/FITEE.2200082

Duan ZM, Wu BW, Wang Y, et al., 2023. A 76-81 GHz 2×8 MIMO radar transceiver with broadband fast chirp generation and 16-antenna-in-package virtual array. *IEEE J Solid-State Circuits*, 58(11):3103-3112. https://doi.org/10.1109/JSSC.2023.3272676

Inanlou F, Coen CT, Cressler JD, 2014. A 1.0 V, 10-22 GHz, 4 mW LNA utilizing weakly saturated SiGe HBTs for single-chip, low-power, remote sensing applications. *IEEE Microwave Wireless Compon Lett*, 24(12):890-892. https://doi.org/10.1109/LMWC.2014.2361662

Kashani MH, Tarkeshdouz A, Afshari E, et al., 2019. A 53-67 GHz low-noise mixer-first receiver front-end in 65-nm CMOS. *IEEE Trans Circuits Syst I: Reg Pap*, 66(6):2051-2063. https://doi.org/10.1109/TCSI.2019.2895893

Kim SK, Cui CL, Huang GC, et al., 2012. A 77 GHz low LO power mixer with a split self-driven switching cell in 65 nm CMOS technology. *IEEE Microwave Wireless Comp Lett*, 22(9):480-482. https://doi.org/10.1109/LMWC.2012.2213076

Kolios V, Kalivas G, 2016. A 60 GHz down-conversion mixer with variable gain and bandwidth in 130 nm CMOS technology. Proc 5th International Conf on Modern Circuits and Systems Technologies, p.1-4. https://doi.org/10.1109/MOCAST.2016.7495147

Krishnamurthy S, Iotti L, Niknejad AM, 2021. Design of high-linearity mixer-first receivers for mm-wave digital MIMO arrays. *IEEE J Solid-State Circuits*, 56(11):3375-3387. https://doi.org/10.1109/JSSC.2021.3101984

Liu ZQ, Dong JY, Chen ZL, et al., 2018. A 62-90 GHz high linearity and low noise CMOS mixer using transformer-coupling cascode topology. *IEEE Access*, 6:19338-19344. https://doi.org/10.1109/ACCESS.2018.2814062

Longhi PE, Pace L, Colangeli S, et al., 2020. V-band GaAs metamorphic low-noise amplifier design technique for sharp gain roll-off at lower frequencies. *IEEE Microwave Wireless Compon Lett*, 30(6):601-604. https://doi.org/10.1109/LMWC.2020.2986927

Mazor N, Sheinman B, Katz O, et al., 2017. Highly linear 60-GHz SiGe down-conversion/up-conversion mixers. *IEEE Microwave Wireless Compon Lett*, 27(4):401-403. https://doi.org/10.1109/LMWC.2017.2678426

Razavi B, 2000. Design of Analog CMOS Integrated Circuits. New York: McGraw-Hill.

Sutbas B, Ng HJ, Wessel J, et al., 2022. A V-band low-power and compact down-conversion mixer with low LO power in 130-nm SiGe BiCMOS technology. Proc 16th European Microwave Integrated Circuits Conf, p.96-99. https://doi.org/10.23919/EuMIC50153.2022.9783953

Vardarli E, Sakalas P, Schröter M, 2022. A 5.9 mW E-/W-band SiGe-HBT LNA with 48 GHz 3-dB bandwidth and 4.5-dB noise figure. *IEEE Microwave Wireless Compon Lett*, 32(12):1451-1454. https://doi.org/10.1109/LMWC.2022.3192488

Wang RT, Zhu W, Wang Y, 2024. An adaptive analog temperature compensated W-Band front-end with ±0.0033 dB/℃ gain variation across-30℃ to 120℃. *IEEE Trans Circuits Syst II: Express Briefs*, 71(2):542-546. https://doi.org/10.1109/TCSII.2023.3313815

Wei HJ, Meng CC, Wang TW, et al., 2012. 60-GHz dual-conversion down-/up-converters using Schottky diode in 0.18 μm foundry CMOS technology. *IEEE Trans Microwave Theory Tech*, 60(6):1684-1698. https://doi.org/10.1109/TMTT.2012.2189412

Wu CL, Yu CK, Kenneth K O, 2015. Amplification of nonlinearity in multiple gate transistor millimeter wave mixer for improvement of linearity and noise figure. *IEEE Microwave Wireless Compon Lett*, 25(5):310-312. https://doi.org/10.1109/LMWC.2015.2409784

Yu YM, Kang K, 2020. Analysis and design of transformer-based CMOS ultra-wideband millimeter-wave circuits for wireless applications: a review. *Front Inf Technol Electron Eng*, 21(1):97-115. https://doi.org/10.1631/FITEE.1900491

Yu YM, Liu RY, Zuo YJ, et al., 2024. A 60-90 GHz mixer-first receiver with adaptive temperature-compensation technique. *IEEE Microwave Wireless Technol Lett*, 34(4):443-446. https://doi.org/10.1109/LMWT.2024.3369652

Unedited